Multiscale Fluid-Phase-Behavior Simulation in Shale Reservoirs Using a Pore-Size-Dependent Equation of State

Sheng Luo, Jodie L. Lutkenhaus, and **Hadi Nasrabadi,** Texas A&M University

Summary

The phase behavior of reservoir fluids plays a fundamental role in predicting well performance and ultimate recovery. The uncertainty in phase behavior is currently one of the greatest challenges in developing unconventional shale resources. The complex phase behavior is attributed to the broad range of pore sizes in shale. In macroscale geometries such as fractures and macropores, the fluid behavior is bulk-like; in nanoscale pores, the fluid behavior is significantly altered by confinement effects. The overall phase behavior of fluids in porous media of mixed pore sizes is yet to be understood.

In this paper, we present a study on the effect of pore-size distribution on the phase behavior of shale-reservoir fluids in a multiscale-pore system. The global fluid-phase equilibria among different sizes of pores are simulated. A pore-size-dependent equation of state (EOS) is used to describe the fluid by the confining pore diameter. The EOS confinement parameters for fluid/pore-wall surface interaction are determined by experimental results from differential-scanning calorimetry (DSC) and isothermal adsorption of species C_{1-14}. The multiscale phase equilibria are simulated by directly minimizing the total Helmholtz free energy. A modified Eagle Ford oil is used for the case study. Constant-composition expansions (CCEs) of dual-scale (bulk and 15 nm) and triple-scale (bulk, 15 nm, and 5 nm) systems are simulated. The first bubble emerges from the bulk region at a lightly suppressed "apparent" bubblepoint pressure. Below the bubblepoint, the liquid saturation in the bulk region drops sharply, but the fluids in the nanopores are undersaturated throughout the multistage expansions. In the end, large amounts of intermediate-to-heavy hydrocarbons are retained in nanopores, implying a significant oil-recovery loss in shale. The confinement effect also leads to near-critical phase behavior in small-scale nanopores (<5 nm).

Introduction

The complex phase behavior of petroleum fluids in shale is currently one of the most challenging problems for shale oil/gas production (Civan et al. 2013). Anomalous production behavior associated with fluid pressure/volume/temperature (PVT) properties has frequently been observed in production from liquid-rich shale (LRS). Du and Chu (2012) and Nojabaei et al. (2013) noted a suppressed bubblepoint and inconsistent laboratory PVT properties compared with the actual gas/oil ratio (GOR) data in Bakken oil production. Whitson and Sunjerga (2012) observed that the LRS producing wellstreams were always much leaner than what would be produced from a conventional reservoir. They found that an initially oil-saturated LRS reservoir will produce significantly less oil than a conventional reservoir under the same drawdown, and the factor of oil recovery from LRS compared with the recovery of conventional oil reservoirs is typically 0.5 to 0.05. The recovery was dependent on initial GOR and the degree of undersaturation, where oil-recovery loss is greatest for near-saturated initial conditions (Whitson and Sunjerga 2012).

The complexities of phase behavior in shale arise from several factors such as pore scale, pore-size distribution, surface properties, and heterogeneity of shale porous geometries (Honarpour et al. 2012; Hu et al. 2014). In hydraulic fractures, natural fractures, and macropores, the confining geometries range from hundreds of nanometers to micrometers (Warpinski 1985; Gale et al. 2007, 2014), where the reservoir fluids are in bulk state. On the other hand, a significant portion of shale porosity is contributed by nanopores, where confinement effects alter the fluid phase behavior from the bulk behavior (Alharthy et al. 2013; Li et al. 2014; Jin and Firoozabadi 2016). Herein, the pore geometries in shale are thermodynamically divided into two categories: macroscale (bulk region) and nanoscale (nanopores).

Physisorption is a widely used method in investigating the fluid phase behavior in nanopores. Adsorption behavior of argon, nitrogen, light hydrocarbons (C_{1-4}), and some intermediate hydrocarbons (C_5, C_6) in nanoporous media have been experimentally studied (Zhu et al. 1999; Kuraoka et al. 2001; Thommes et al. 2002). It is generally observed that the adsorption pore filling happens at a very low relative pressure (p/p^o) in pores of less than 2 nm because the proximity of pore surfaces results in strong interaction between the adsorbate and pore surface. Pore filling later happens at an increased p/p^o in pores with diameter larger than 2 nm, and both monolayer/multilayer adsorption and capillary condensation may be observed. Finally, in very large pores (diameter > approximately 50 nm), pore filling occurs near or at $p/p^o = 1$; i.e., phase behavior is almost the same as bulk (Sing et al. 1985). On the basis of this, the International Union of Pure and Applied Chemistry adopts the notations that (Sing et al. 1985; Rouquerol et al. 1994) a micropore has pore diameter < 2 nm; mesopores are 2 nm < pore diameter < 50 nm; and a macropore has pore diameter > 50 nm. Luo et al. (2015, 2016a, b, c) developed an isobaric measurement of DSC for the phase transitions in nanopores. The liquid/vapor phase-transition temperatures of intermediate-to-heavy hydrocarbons (C_5 and greater) in nanopores (diameter of 2.0 to 37.9 nm) have been measured. It was observed that at 37.9 nm, the confinement effect was negligible, and that the decreased pore diameter resulted in an increased bubblepoint temperature until the pore diameter was smaller than approximately 4 nm, where the fluid entered a supercritical state and pore-vaporization behavior sharply changed (Luo et al. 2016a). Alternative experimental techniques include nuclear magnetic resonance (Naumov et al. 2008), small-angle X-ray diffraction (Günther et al. 2008), neutron diffraction (Floquet et al. 2007), and visual observation (Alfi et al. 2016). As observed in experiments, fluids show bulk phase behavior in pores larger than 50 nm, whereas in nanopores smaller than 50 nm, the phase behavior is distinctly altered by the confinement effect. Herein, we note the pore geometries of different scales in shale as the bulk region (fractures, macropores), with pore diameters > 50 nm, and nanopores, with pore diameters < 50 nm.

Theoretical studies and simulation work on phase behavior in nanopores have been performed in many aspects. The Kelvin equation describes the phase equilibrium by defining a vapor/liquid phase-pressure difference (i.e., capillary pressure) using the Young-Laplace equation, where it is assumed that the liquid/vapor interface is smooth and homogeneous and that the surface tension is equal to that in the bulk. Several studies examined the nanoscale fluid-phase behavior by implementing the capillary pressure in flash calculations using the Peng-Robinson EOS (PR EOS) (Peng and Robinson 1976; Alharthy et al. 2013; Nojabaei et al. 2013; Dong et al. 2016; Wang et al. 2016; Zhang et al. 2017). Tan and Piri (2015a, b) reported EOS modeling by perturbed-chain statistical associating fluid theory coupled with a modified Young-Laplace equation. Density function theory (DFT) (Li et al. 2014; Jin and Firoozabadi 2016) and molecular-simulation (Singh et al. 2009, 2010; Singh and Singh 2011; Jin and Nasrabadi 2016) studies have brought substantial insight into the phase transitions in nanopores. Both techniques simulate the fluid in nanopores using the fundamental descriptions of molecular fluid/fluid and fluid/pore surface interactions. Li et al. (2014) developed an engineering DFT technique combined with PR EOS and simulated adsorptions of single components and hydrocarbon mixtures in nanoscale slit pores. Jin and Nasrabadi (2016) presented a gauge-grand-canonical Monte Carlo (gauge-GCMC) molecular simulation to study phase equilibria of single and multicomponent hydrocarbons and found that, in nanopores, the critical temperature is reduced and the density gap between liquid and vapor phase is narrowed. Jin and Firoozabadi (2016) comparatively applied the methods of the Langmuir adsorption isotherm, solid/solution model, PR EOS/capillary pressure, DFT, and grand-canonical Monte Carlo (GCMC) molecular simulation to model the phase behavior of hydrocarbons in shale, and suggested that in pores with sizes greater than 10 nm, the conventional EOS may be applicable, whereas in pores smaller than 10 nm, the fluids become inhomogeneous and molecular-level modeling is necessary.

A novel pore-size-dependent EOS [PR-Confined (PR-C) EOS] was presented by Travalloni et al. (2010a, b, 2014). The PR-C EOS uses molecular descriptions of fluid/fluid and fluid/pore-surface interactions, and it relates the fluid PVT behavior to the fourth dimension of confining-pore diameter. The EOS requires two confinement parameters of range and energy to describe the fluid/pore-surface interaction. In these previous studies, the PR-C EOS has been applied to describe confinement effects for a simplified case of nanoporous media and single- or binary-fluid systems. To date, it is not clear if this approach is appropriate for more-realistic cases, such as for reservoir fluids in a multiscale system.

In this paper, we report an approach to simulate the phase behavior of multicomponent reservoir fluids in multiscale pore systems in an effort to understand fluid-phase behavior in the shale tight formations with broad pore-size distribution. First, a multiscale phase-behavior model is presented. Next, we show a pore-size-dependent methodology to describe each geometric scale under pore diameter. The confinement parameters for various hydrocarbons (C_{1-14}) serve as the database to determine the parameters for hydrocarbon species. Direct minimization of the total Helmholtz free energy is used to calculate the multiscale phase equilibrium. Finally, we perform a case study of CCEs using a modified Eagle Ford shale oil. PVTs of single-scale (bulk), dual-scale (bulk and 15 nm), and triple-scale (bulk, 15 nm, and 5 nm) systems are simulated. The fluid PVT relations and compositions are discussed in relation to their effects on oil production.

Multiscale Phase-Behavior Model

The scales of porous geometries in shale reservoirs range across several orders of magnitude. Natural fractures are commonly found to have the widths of a few micrometers to millimeters (Anders et al. 2014; Gale et al. 2014). After hydraulic-fracture stimulation, macro-scale fractures are introduced to the formation in connection to the wellbore (Warpinski 1985), and a significant amount of natural microfractures are reactivated (Dahi-Taleghani and Olson 2011). Within the shale matrix, the pore sizes are in the range of nanometers to micrometers. The matrix pores are classified into mineral pores and organic-matter pores. The mineral pores are in micrometers, and the organic-matter pores range from a few to hundreds of nanometers, although the organic-matter bubble pores can be a few micrometers (Loucks et al. 2009; Ko et al. 2017). The actual pore-size distributions usually vary from case to case (Honarpour et al. 2012; Kuila and Prasad 2013). Cho et al. (2016) comparatively measured the pore sizes of shale samples by mercury-injection capillary pressure and discovered several pore-size-distribution patterns. The middle Bakken Shale exhibits a unimodal pore-size distribution (30 to 50 nm) or a bimodal pore-size distribution (30 and 100 nm). For the Niobrara Formation, the pore-size distributions are mostly unimodal, and the pore diameters range from 4 to 11 nm. Ko et al. (2017) presented a quantitative analysis of pore structures with Eagle Ford Shale samples using different analytical methods. Using scanning-electron-microscope (SEM) imaging and pore tracing, they identified that the pore diameters distribute bimodally at 10 to 30 nm and 35 to 1000 nm. However, the SEM/pore-tracing method is limited to resolving pore diameters from approximately 20 nm to 15 μm (**Fig. 1,** blue columns). Nitrogen adsorption is able to measure pores with diameters of 0.3 to 200 nm, and the measurement shows significant volumetric portions of nanopores smaller than 10 nm (Fig. 1, red columns) (Ko et al. 2017). SEM/pore-tracing and nitrogen-adsorption analyses combine to form the whole picture of pore-size distribution: Both nanopores and macropores constitute important porosities in the Eagle Ford Shale.
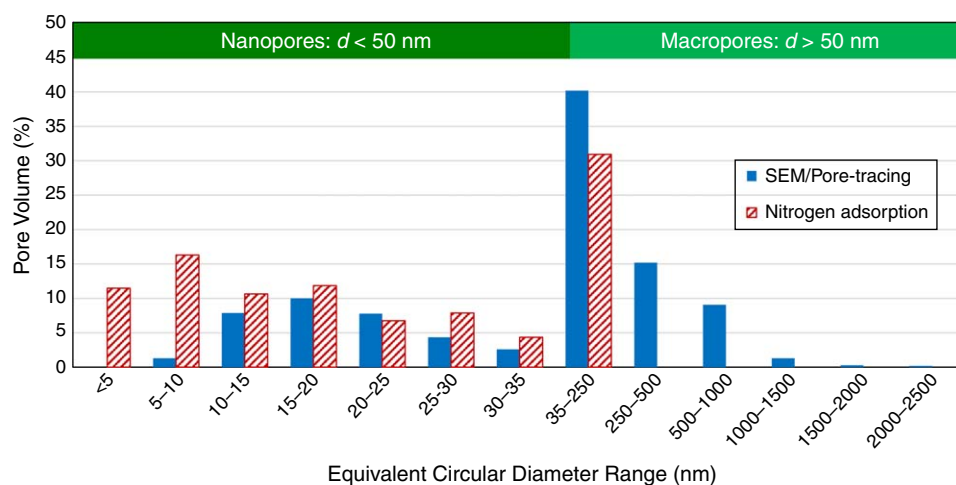

Fig. 1—Pore-size distribution of an upper Eagle Ford core by SEM/pore-tracing and nitrogen-adsorption analyses (Ko et al. 2017). The SEM/pore-tracing method resolves pore diameters from approximately 20 nm to 15 μm, and nitrogen adsorption measures pores from 0.3 to 200 nm. The combination of results from the two methods forms the whole picture of pore-size distribution (1 μm = 1000 nm).

A multiscale model of fluid in shale is conceived using distinct phase behaviors under different confining scales; the porous space is divided into a bulk region and nanopores **(Fig. 2).** The bulk region refers to the hydraulic fractures, natural fractures, and macropores in the shale matrix, where the reservoir fluid behaves as bulk fluid; the nanopores are the pores in the matrix with a diameter less than 50 nm, where the phase behavior deviates from the bulk. Because of the strong confinement in small nanopores (<10 nm) but weak confinement above 30 nm (Luo et al. 2016a), the nanoporosity is further discretized into pores of several diameters ($d_1, d_2, d_3, ...$). The multiscale phase-behavior model is analogous to the dual/multiple-porosity (permeability) model (Warren and Root 1963; Gilman and Kazemi 1983), whereas in this model, we specifically investigate the thermodynamic phase equilibria among pore geometries of multiple scales. In this model, the PVT relation and fluid compositions in nanopores and in the bulk region are dependent on the global phase equilibrium.
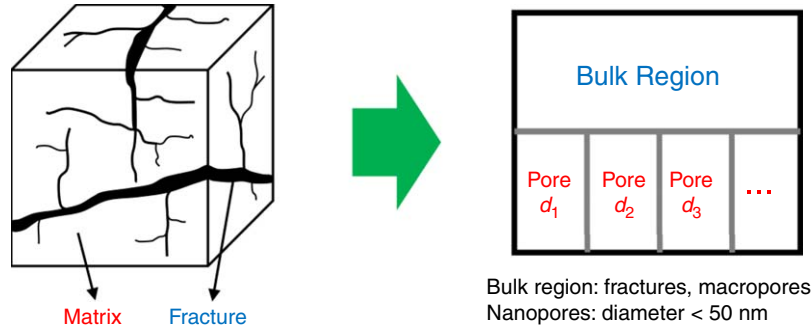

Fig. 2—Multiscale model for fluid-phase behavior in fractured-shale reservoirs. The shale porous space is divided into the bulk region, where the fluid shows bulk behavior, and nanopores, where the fluid-phase behavior is altered under the nanoconfinement effect. The phase behavior of the whole system is the thermodynamic equilibria among the bulk region and multiple sizes of nanopores.

Herein, we simulate the depletion of the shale reservoir by modeling the CCE of the multiscale system. The bulk region volume is repeatedly expanded, but the volumes of nanopores are fixed at the initial condition because the volumetric flow primarily takes place through the bulk-scale geometries such as fractures, whereas the transmissivity from small pores is very low (Bear et al. 1993; Choi et al. 1997).

We consider the isothermal/isochoric fluid-phase equilibria among the bulk region and NP sizes of nanopores with pore diameters noted as $d_1, d_2, ..., d_{NP}$. The multiscale system is defined with given moles of NC components ($n_1, n_2, ..., n_{NC}$), volumes (bulk region volume V_b and volumes of nanopores $V_1, V_2, ..., V_{NP}$), and temperature (T). The numbers of fluid phases are noted as NF_b phases in the bulk region and NF_k phases in the nanopore of diameter $d_k (k = 1, 2, ..., NP)$. The total Helmholtz free energy (A) is the sum of the bulk region and all nanopores (Eqs. 1 through 3). The constraints are the conservations of moles and regional volumes (Eqs. 4 through 6), where i denotes the properties of component i and j denotes the properties for phase j.

The total Helmholtz free energy of the bulk NP nanopores system is

$$A = A_b + \sum_{k=1}^{NP} A_{p,k}, \quad \dots\dots\dots\dots\dots\dots\dots\dots\dots\dots\dots\dots\dots\dots\dots\dots\dots\dots\dots \quad (1)$$

$$A_b = \sum_{j=1}^{NF_b} \left(-P_{j,b} V_{j,b} + \sum_{i=1}^{NC} n_{ij,b} \mu_{ij,b} \right), \quad \dots\dots\dots\dots\dots\dots\dots\dots\dots\dots\dots\dots\dots\dots \quad (2)$$

$$A_{p,k} = \sum_{j=1}^{NF_k} \left(-P_{j,k} V_{j,k} + \sum_{i=1}^{NC} n_{ij,k} \mu_{ij,k} \right). \quad \dots\dots\dots\dots\dots\dots\dots\dots\dots\dots\dots\dots\dots \quad (3)$$

The constraints are molar and volumetric conservations:

$$\sum_{j=1}^{NF_b} V_{j,b} = V_b, \quad \dots\dots\dots\dots\dots\dots\dots\dots\dots\dots\dots\dots\dots\dots\dots\dots\dots\dots\dots\dots\dots\dots \quad (4)$$

$$\sum_{j=1}^{NF_k} V_{j,k} = V_k \qquad \forall k \in \{1, 2, ..., NP\}, \quad \dots\dots\dots\dots\dots\dots\dots\dots\dots\dots\dots\dots \quad (5)$$

$$\sum_{j=1}^{NF_b} n_{ij,b} + \sum_{k=1}^{NP} \sum_{j=1}^{NF_k} n_{ij,k} = n_i. \quad \dots\dots\dots\dots\dots\dots\dots\dots\dots\dots\dots\dots\dots\dots\dots\dots \quad (6)$$

Under isothermal conditions,

$$T_b = T_{p,1} = T_{p,2} = ... = T_{p,NP}. \quad \dots\dots\dots\dots\dots\dots\dots\dots\dots\dots\dots\dots\dots\dots\dots\dots\dots \quad (7)$$

The global phase equilibrium of the multiscale system can be determined as the state of minimized Helmholtz free energy (Cabral et al. 2005; Travalloni et al. 2014; Firoozabadi 2015). At the first-order optimality conditions, the system naturally satisfies the equality of chemical potentials for any component i among phases from all regions and equality of pressures among phases within each region:

$$\mu_{i,b} = \mu_{i,1} = \mu_{i,2} = ... = \mu_{i,NP}, \quad \dots\dots\dots\dots\dots\dots\dots\dots\dots\dots\dots\dots\dots\dots\dots\dots\dots \quad (8)$$

$$\mu_{i,b} = \mu_{ij,b} \quad \forall j \in \{1,2,...,NF_b\}, \quad \dots \dots \dots \dots \dots \dots \dots \dots \dots \dots \dots \dots \dots \dots \quad (9)$$

$$\mu_{i,k} = \mu_{ij,k} \quad \forall j \in \{1,2,...,NF_k\} \text{ and } \forall k \in \{1,2,...,NP\}, \quad \dots \dots \dots \dots \dots \dots \dots \dots \dots \dots \quad (10)$$

$$P_{1,b} = P_{2,b} = ... = P_{NF_b,b}, \quad \dots \dots \dots \dots \dots \dots \dots \dots \dots \dots \dots \dots \dots \dots \dots \dots \dots \quad (11)$$

$$P_{1,k} = P_{2,k} = ... = P_{NF_k,k} \quad \forall k \in \{1,2,...,NP\}. \quad \dots \dots \dots \dots \dots \dots \dots \dots \dots \dots \dots \dots \quad (12)$$

Pore-Size-Dependent EOS Strategy

The multiscale system requires a specific description of fluid phase behavior for each pore scale, where a pore-size-adaptable EOS is ideal. Travalloni et al. (2014) presented a PR-C EOS extended from the PR EOS by the generalized van der Waals theory (Vera and Prausnitz 1972; Sandler 2010). The PR-C EOS considers the interaction between the fluid and pore surface as a square-well potential **(Fig. 3),** where two parameters of square-well depth (ε_p) and square-well width (δ_p) need to be determined by experiments. The method of directly considering fluid/pore-surface interaction is in agreement with the molecular-interaction treatments in molecular simulation and DFT, and the formulations yield the explicit expression of fluid chemical potential in nanopores (Eq. 14). The EOS describes the fluid in pores with a parameter of cylindrical pore diameter (d_p) and it reverts to PR EOS at the large pore diameter. The pore-size-dependent nature brings convenience in solving the multiscale phase equilibria with one unified EOS.
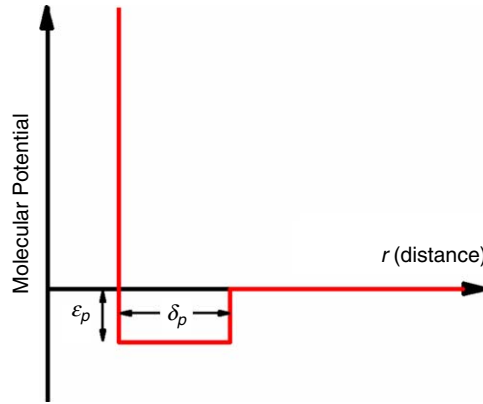

Fig. 3—Square-well potential model for the fluid/pore-surface interaction. ε_p is the square-well depth; δ_p is the square-well width. ε_p and δ_p need to be determined by experiments.

The PR-C EOS is written as follows (Travalloni et al. 2014):

$$P = \frac{RT}{v - b_p} - \frac{a_p}{v^2 + 2b_p v - b_p^2} - \sum_{i=1}^{NC} \left(\frac{x_i^2 \theta_i b_{p,i}}{v^2} \left(1 - \frac{x_i b_{p,i}}{v}\right)^{\theta_i - 1} (1 - F_{pr,i}) \left\{ RT \left[1 - \exp\left(-\frac{N_{av}\varepsilon_{p,i}}{RT}\right)\right] - N_{av}\varepsilon_{p,i} \right\} \right). \quad \dots \dots \quad (13)$$

$$\mu_i = \mu_{0,i} + RT\ln\left(\frac{N_{av}x_i \lambda_i^3}{v - b_p}\right) + \frac{RTb_{p,i}}{v - b_p} - \frac{a_p b_{p,i} v}{b_p(v^2 + 2b_p v - b_p^2)} + \frac{\sqrt{2}}{4}\ln\left[\frac{v + (1+\sqrt{2})b_p}{v + (1-\sqrt{2})b_p}\right]\left[\frac{a_p b_{p,i}}{b_p^2} - \frac{2}{b_p}\sum_{j=1}^{NC}(x_j a_{p,ij})\right] - F_{pr,i}N_{av}\varepsilon_{p,i}$$

$$+ \left[1 - (\theta_i + 1)\frac{x_i b_{p,i}}{v}\right]\left(1 - \frac{x_i b_{p,i}}{v}\right)^{\theta_i - 1}(1 - F_{pr,i})\left\{RT\left[1 - \exp\left(-\frac{N_{av}\varepsilon_{p,i}}{RT}\right)\right] - N_{av}\varepsilon_{p,i}\right\}. \quad \dots \dots \dots \dots \dots \quad (14)$$

Herein, we have developed a multiscale PVT model with PR-C EOS. The volume shift is applied (see section Case Description for volume-shift parameters). The total Helmholtz free energy of the multiscale system (Eq. 1) is expressed by Eqs. 13 and 14. The multiscale phase equilibrium is calculated by directly minimizing the Helmholtz free energy with the tunneling global optimization method (Nichita et al. 2002, 2006). The phases in the bulk region/nanopores are split or combined depending on stability analysis. The inputs are moles of components, volumes of multiscale regions, and temperature. The outputs are the fluid compositions and pressure in each region of scale at phase equilibrium.

EOS Confinement Parameters

The confinement parameters of square-well depth (ε_p) and width (δ_p) for fluid/pore-surface interactions are required to be determined from experiments. We developed an isobaric measurement of DSC for fluid in nanopores (Luo et al. 2015), and the phase transition temperatures of *n*-hexane, *n*-octane, and *n*-decane were measured in pores from 2.0 to 37.9 nm. The confinement parameters of ε_p and δ_p were determined accordingly. The phase boundaries between liquid, vapor, and supercritical fluid predicted by PR-C EOS overlap very well with experimental findings (Luo et al. 2016a). Recently, we measured the phase transitions of intermediate-to-heavy hydrocarbons in nanopores and obtained the confinement parameters (ε_p, δ_p) for C_{5-14}. For the light hydrocarbons (C_{1-4}), the parameters were determined by fitting the adsorption isotherms in nanoporous media (Kuraoka et al. 2001; Matsumoto et al. 2004, Lourenço et al. 2016).

In calculating the confinement parameters by experimental data, we observed that for a specific species, ε_p and δ_p are in negative correlation and the product (area of square well) is positively correlated to molecular weight. Therefore, we suggest a normalized fluid/pore-surface affinity factor, κ, as the product of ε_p and δ_p over molecular weight (Eq. 15). The κ factor describes the interaction strength between the fluid and pore surface per molecular weight. On a given surface, the κ factor should be dependent on the fluid molecular

structure. The κ factor relation to molecular weight of n-alkanes is shown in **Fig. 4.** In practice, it is suggested that $\delta_p/\sigma = 0.5$, in agreement with the set in molecular simulations (Carley 1983; Chapela et al. 1987), because a ratio that is too large or too small may lead to deviated phase equilibrium (Vega et al. 1992). The hydrocarbon-confinement parameters are listed in the section Case Description.

Fluid/pore-surface affinity factor is given as $\kappa = \dfrac{\varepsilon_p \cdot \delta_p}{MW}$. . . . . (15)
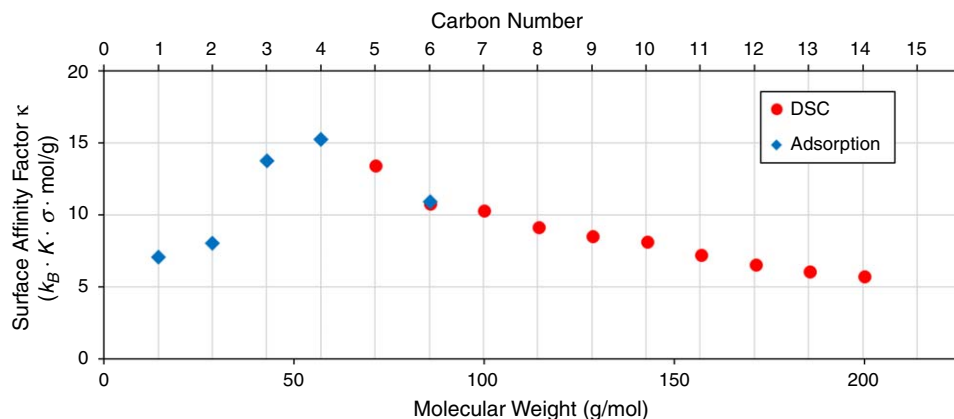
Fig. 4—Fluid/pore-surface affinity factor κ in relation to molecular weight and carbon number of n-alkanes. ε_p is defined with the unit of $k_B \cdot K$ (k_B is the Boltzmann constant) and δ_p is defined with the unit of fluid molecular diameter (σ). Confinement parameters for C_{1-4} and C_6 are obtained by fitting the adsorption isotherms in nanopores with diameters of 2.4 to 3.8 nm (Kuraoka et al. 2001; Matsumoto et al. 2004; Lourenço et al. 2016). Parameters for C_{5-14} are determined by the liquid/vapor phase transition temperature in the 6.0-nm pore, measured by DSC. All experimental measurements used nanoporous silica with silylated surface.

It is worth noting that the confinement parameters in Fig. 4 are determined from the DSC/adsorption experiments with silylated nanoporous silica. The silylation modification renders organic characteristics to the media surface, which are experimentally observed as hydrophobicity (nonwater-wet) and oleophilicity (oil-wet) (Zhao and Lu 1998). The silylated surface makes the experimental nanoporous media a reasonable analog to organic matter, where most nanopores are located in shale (Loucks et al. 2009; Ko et al. 2017).

Case Description

We use a case of modified black oil from the Eagle Ford LRS by Orangi et al. (2011). The reservoir fluids are grouped into six pseudocomponents. The components' mole fractions in **Table 1** are used as the feed (i.e., total mole fractions) to the multiscale system (Fig. 2). The PR-C EOS parameters are listed in **Tables 1 and 2,** where the critical properties, acentric factors, volume-shift parameters, and binary-interaction parameters are bulk species parameters. The confinement parameters ε_p and δ_p of the pseudocomponents are obtained by interpolation or extrapolation using the κ-factor/molecular-weight plot in Fig. 4 (assuming $\delta_p/\sigma = 0.5$).

Species	MW (g/mol)	T_C (°R)	P_C (psia)	ω	VSP	ε_p/k_B (K)	δ_p/σ	Mole Fraction
N_2-C_1	16.07	343.02	672.70	0.01306	−0.15403	227	0.5	0.31304
C_2	30.07	549.80	708.40	0.09860	−0.10020	481	0.5	0.04314
CO_2-C_3	44.08	644.14	690.06	0.16954	−0.08303	1,209	0.5	0.05430
C_{4-6}	72.04	839.26	488.86	0.24541	−0.03861	1,932	0.5	0.13301
C_{7-10}	114.40	1,060.50	402.80	0.37390	0.01910	2,091	0.5	0.16297
C_{11+}	238.07	1,391.01	234.71	0.67743	0.18412	2,407	0.5	0.29354

Table 1—PR-C EOS properties for Eagle Ford oil modified from Orangi et al. (2011). MW = molecular weight; VSP = volume-shift parameter.

	N_2-C_1	C_2	CO_2-C_3	C_{4-6}	C_{7-10}	C_{11+}
N_2-C_1	0.000	0.000	0.005	0.021	0.038	0.077
C_2	0.000	0.000	0.004	0.018	0.034	0.072
CO_2-C_3	0.005	0.004	0.000	0.006	0.016	0.045
C_{4-6}	0.021	0.018	0.006	0.000	0.002	0.019
C_{7-10}	0.038	0.034	0.016	0.002	0.000	0.008
C_{11+}	0.077	0.072	0.045	0.019	0.008	0.000

Table 2—Binary-interaction parameters for Eagle Ford oil modified from Orangi et al. (2011).

The reservoir conditions are presented in **Table 3** (Orangi et al. 2011). The shale-oil reservoir is initially undersaturated at 6,000 psia at 240°F. The ratio between the bulk region volume and nanopore volume (diameter < 50 nm) should be dependent on the exact formation and also the specific location within the reservoir. Ko et al. (2017) showed that for Eagle Ford Shale, the bulk region volume is similar to the volume of nanopores (Fig. 1). Herein, we use 1:1 as the representative initial volume ratio of the bulk region to the nanopores, except for the single-scale case, where all the space is assigned as bulk.

Properties	Value
Reservoir temperature	240°F
Initial reservoir pressure	6,000 psia
Initial $V_{bulk}/V_{nanopores}$	1:1
Reservoir-fluid type	Oil

Table 3—Reservoir conditions of an Eagle Ford LRS.

In simulating the CCE, the bulk region volume is repeatedly expanded while the volumes of nanopores are kept constant because the volumetric flow mainly takes place through the bulk-scale geometries (e.g., fractures) (Bear et al. 1993; Choi et al. 1997). The bulk region is given a typical macropore diameter of 10 μm. The diameters of nanopores are specified as 5 or 15 nm, depending on the nanoscale pore-size distribution of Eagle Ford Shale (Fig. 1). The sensitivity analysis of bubblepoint to the bulk/nanopore-volume ratio is studied in the end.

Results and Discussions

Single-Scale PVT (Conventional Reservoirs). The PVT model using PR-C EOS is first validated by simulating the fluid PVT at the single bulk scale—i.e., the conventional reservoir conditions. The single-scale system is set up with a bulk pore diameter of 10 μm. The phase diagram and pressure/volume relations are calculated. The results from our model match with the simulation output of commercial software using PR EOS (**Fig. 5**). The bubblepoint pressure of the bulk fluid is 2,074 psia. In the following discussions, the single bulk-scale PVT is referred to as conventional reservoir phase behavior.
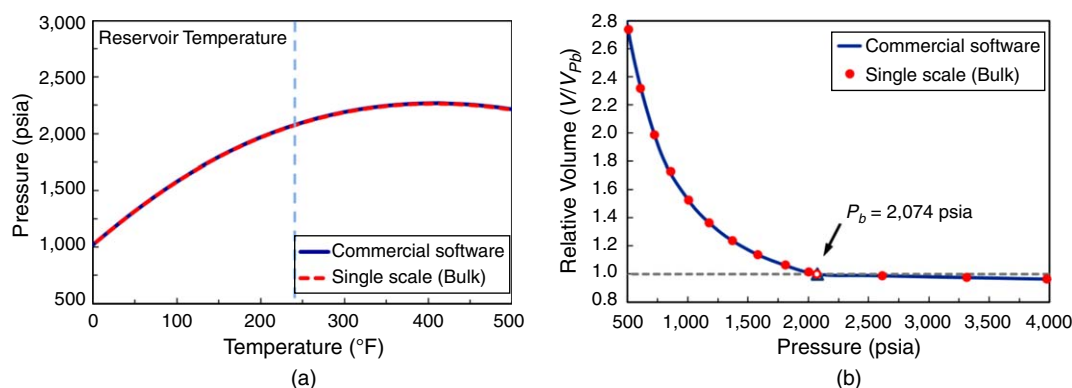

Fig. 5—(a) Phase diagram and (b) pressure/volume plot. The red dashed lines in Fig. 5a and the red round symbols in Fig. 5b show the results from the PR-C EOS PVT model using a single bulk size (pore diameter of 10 μm). In Fig. 5b, the open symbol marks the bubblepoint pressure. The results agree with the output by a commercial software using PR EOS (solid blue lines).

Dual-Scale PVT. The dual-scale CCE is simulated using the multiscale PR-C EOS model. The bulk-scale size is 10 μm, and the nanopore diameter is specified as 15 nm (**Fig. 6**), representing a major nanopore diameter from the Eagle Ford Shale pore-size distribution in Fig. 1 (Ko et al. 2017). The initial volumes of the bulk region and nanopores are assumed to be equal. The bulk region volume is expanded, whereas the nanopore volume is fixed to consider that most volumetric flows take place through the bulk geometries (Bear et al. 1993). The mole fractions in Table 1 serve as the feed to the multiscale system. The system is initially assigned with the same fluid compositions in all regions, and by minimizing the total Helmholtz free energy, the compositional distributions at phase equilibria are calculated. Because of the weak confinement effect at 15 nm, the fluid compositions are slightly different between the bulk region and the 15-nm pores at 6,014 psia (**Fig. 7**).

The molar density profiles of the simulated CCE are shown in Fig. 7. The first bubble forms in the bulk region at 2,002 psia, which is lower than the conventional reservoir bubblepoint (2,074 psia). At the undersaturated conditions ($P > 2,002$ psia), the fluids in both the bulk region and nanopores are in the liquid state, and the molar density is slightly higher in nanopores. There are some small compositional differences: the molar densities of C_2, CO_2-C_3, and C_{4-6} are higher in nanopores than in the bulk region, and these species are associated with relatively large surface-affinity factors (Fig. 4). As the pressure falls below the bubblepoint (2,002 psia), the gas phase expands in the bulk region; the nanopores release the light hydrocarbons (**Fig. 8a**), but retain the intermediate to heavy components (C_{7-10}, C_{11+}) (Figs. 7 and 8c). It is rationalized that the phase mole fraction of C_{11+} in nanopores drops in the undersaturated depletion stage because of the expansion of the bulk region, but it increases below the bubblepoint as the bulk-vapor phase strongly extracts the light components from the nanopores (Fig. 8c). Intermediates C_{4-6} are not released into the bulk-gas phase from 15-nm pores until the pressure falls below approximately 300 psia (Fig. 8b). Because of the confinement effect and accumulations of heavy components (Fig. 8c), the fluid in the nanopores remains undersaturated both above and below the bubblepoint. The liquid phase in the bulk region undergoes a compositional shift toward the heavier side in a similar manner with the liquid in nanopores (Fig. 7). Assuming an ultimate recovery at the pressure of 501 psia (Fig. 7), the nanopores retain large amounts of intermediate to heavy hydrocarbons, which indicates a significant oil loss in shale nanopores.
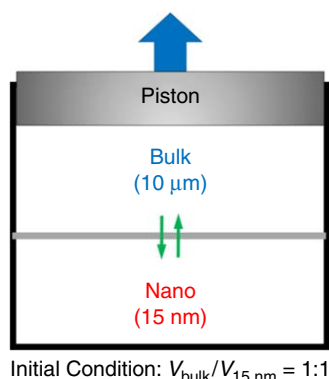
Fig. 6—Dual-scale model (bulk and 15 nm) for CCE. The bulk region is given a pore diameter of 10 µm, and the nanopores are specified with the diameter of 15 nm. The initial volumes of the bulk region and nanopores are assumed equal. The bulk space is expanded, and the volume of nanopores is fixed. The component exchange between the bulk region and nanopores is enabled for global phase equilibrium at each stage (1 µm = 1000 nm).
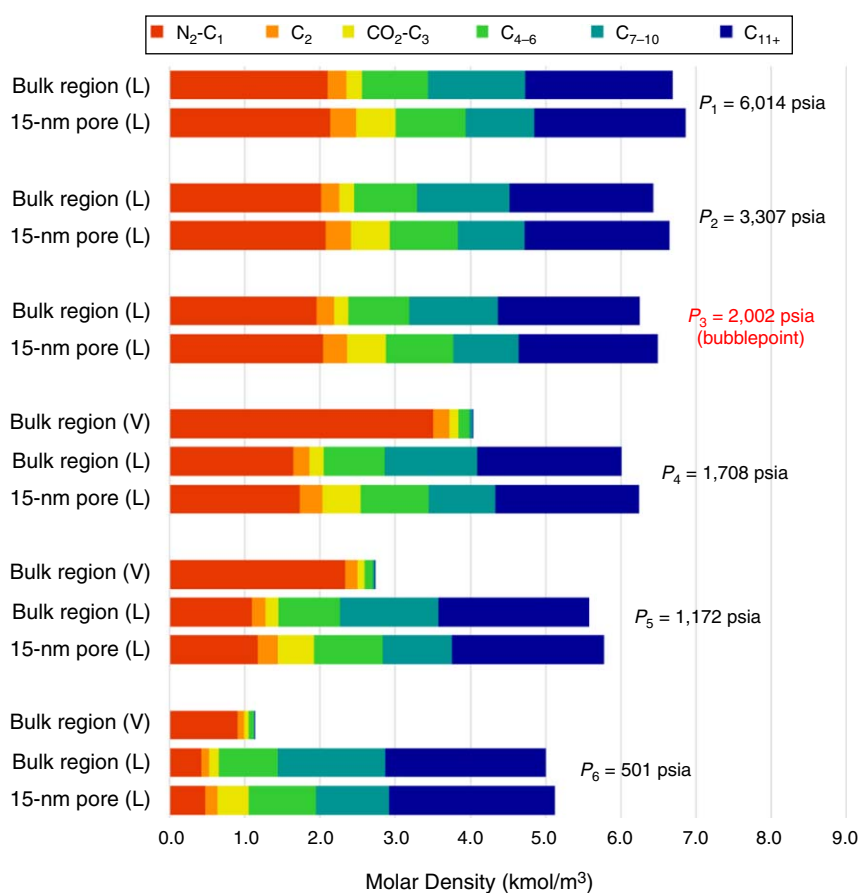

Fig. 7—Molar-density profiles of all phases at selected pressures in the dual-scale CCE. The length of a cylinder section refers to the actual molar density ($kmol/m^3$) of a specific species in the corresponding phase. The noted pressure is the bulk-region pressure. The bubblepoint pressure is 2,002 psia (72 psia lower than the conventional reservoir fluids), and the first bubble emerges from the bulk region. As the pressure is lowered, the gas phase expands in the bulk region, but in 15-nm nanopores, the fluid is always undersaturated. In the end, a significant amount of intermediate and heavy components are trapped in nanopores.

The liquid volumetric saturation of the dual-scale shale system is compared with that of conventional reservoir fluids in **Fig. 9a.** In nanopores, the reservoir fluid is always liquid. The bubblepoint is slightly suppressed, and the liquid saturation in the bulk region quickly declines with decreasing pressure. The liquid saturation in the bulk region is generally lower (5 to 15%) than those in conventional reservoirs. In the oil production from shale, the fast decline of liquid saturation should lead to a sharp rise of GOR once entering the two-phase stage. This can be correlated to the observations by Jones (2017) that in LRS production a quick rise of GOR occurs after the flowing bottomhole pressure falls below the bubblepoint. The pressure/volume relation is plotted in Fig. 9b. The volume of shale nanopores is fixed, and the bulk region volume expands faster with decreasing pressure than it does in the conventional reservoir.
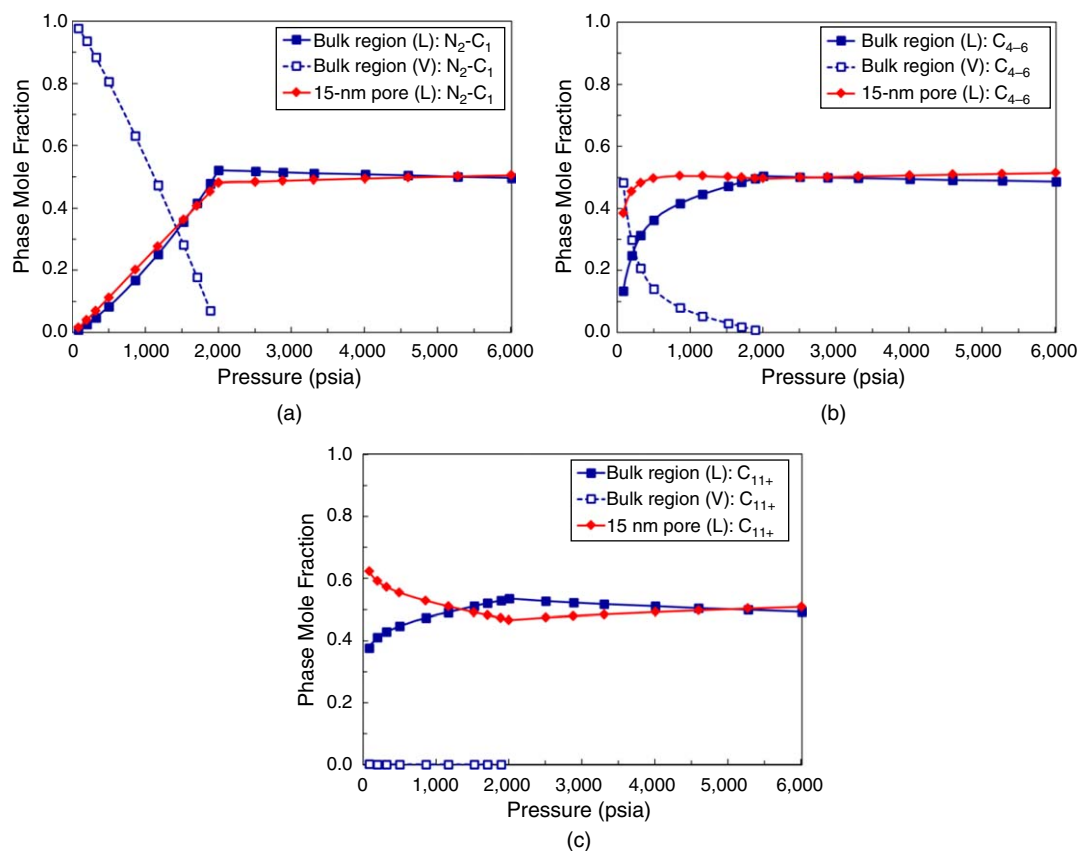
Fig. 8—Phase mole fractions of (a) light component, N$_2$-C$_1$, (b) intermediate component, C$_{4-6}$, and (c) heavy component, C$_{11+}$, distributed in various phases during the dual-scale CCE. The bubblepoint pressure is 2,002 psia. Below the bubblepoint, N$_2$-C$_1$ is quickly released from the bulk- and confined-liquid phases into the bulk-gas phase, and C$_{4-6}$ is released into the gas phase from the nanopores at a very low pressure (approximately 300 psia). C$_{11+}$ accumulates in the liquid phase of the nanopores below the bubblepoint. The phase mole fraction relates to the mole fraction of a species distributed in a certain phase.
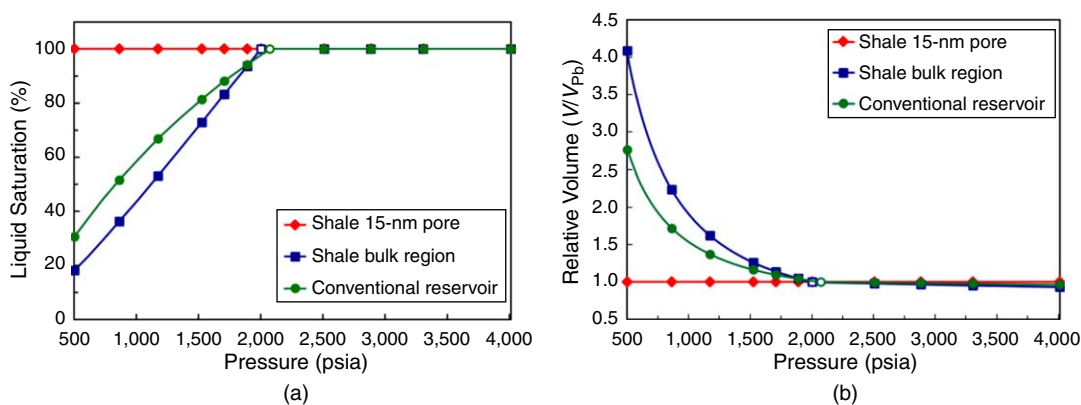

Fig. 9—(a) Liquid volumetric saturation of each region in relation to pressure. In the bulk region, P_b is slightly suppressed, and at the two-phase stage, the liquid saturation drops faster than that in the conventional reservoir. In nanopores (15 nm), the fluids are undersaturated at all pressures. (b) Pressure/volume relations. The nanopore volume is fixed. The bulk region expands with lowered pressure at a rate faster than that in conventional reservoirs. The bubblepoint pressure for shale is marked as an open blue square, and for conventional reservoirs it is marked as a green circle.

Triple-Scale PVT and Criticality. As shown by nitrogen porosimetry (Fig. 1), there is a significant amount of small nanopores (diameter < 10 nm) in shale (Ko et al. 2017). To consider this, we refine the model by introducing the 5-nm pores in the nanopores region. The initial volume ratio is specified as 3:2:1 for the bulk region pores, 15-nm pores, and 5-nm pores **(Fig. 10).** In the same manner with the dual-scale CCE, the bulk volume is expanded, but the volumes of nanopores are fixed. Under the same total feed in Table 2, the initial fluid distributions at 6,002 psia are quite different between the 5-nm pore and the rest of the regions. Because of the strong confinement effect, the fractions of light-to-intermediate components are much higher in 5-nm pores **(Fig. 11).**

The molar density profiles of the triple-scale CCE are shown in Fig. 11. The bubblepoint pressure is 1,936 psia, and the first bubble occurs in the bulk region, which is similar to the behavior in the dual-scale CCE. Above the bubblepoint, fluids in all regions are in the liquid state. However, the compositions in 5-nm pores significantly deviate from those in 15-nm pores and the bulk region. The mole percentages of light and intermediate species are high in the 5-nm pores, but the mole percentage of the heavy component (C$_{11+}$) is relatively low (Fig. 11). The fluid in the 5-nm pores is classified as volatile oil. The fluids in the bulk region and 15-nm pores are typical

black oil by composition. As the pressure decreases below the bubblepoint, the gas phase in the bulk region expands and gathers a great portion of light components (N_2-C_1, C_2) (**Fig. 12a**). The fluids in nanopores become further undersaturated by releasing the light components and accumulating the intermediate to heavy components (Figs. 11, 12b, and 12c). During the two-phase stage (of the bulk region), the compositional change in the 5-nm pores shifts the fluid type from volatile oil toward black oil. Assuming the ultimate recovery pressure as 500 psia (Fig. 11), large amounts of intermediate and heavy hydrocarbons are trapped in the 5- and 15-nm pores.
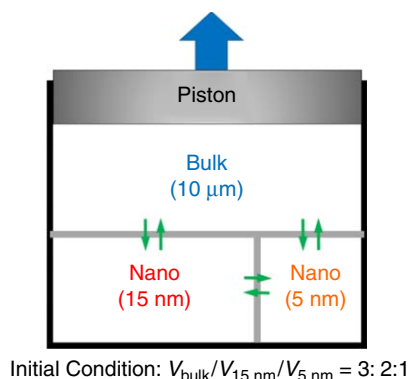

Initial Condition: $V_{bulk}/V_{15\,nm}/V_{5\,nm}$ = 3: 2:1

Fig. 10—Triple-scale model (bulk, 15 nm, and 5 nm) for CCE. The bulk region is given a pore diameter of 10 µm, and the nanopores are specified with the diameters of 15 and 5 nm. The initial volumes of the bulk region pores and the 15- and 5-nm nanopores are assumed as 3:2:1. The bulk space is expanded, and the volumes of nanopores are fixed. The component exchanges between the bulk-region pores and the 15-nm, and 5-nm pores are enabled for global phase equilibrium at each stage (1 µm = 1000 nm).
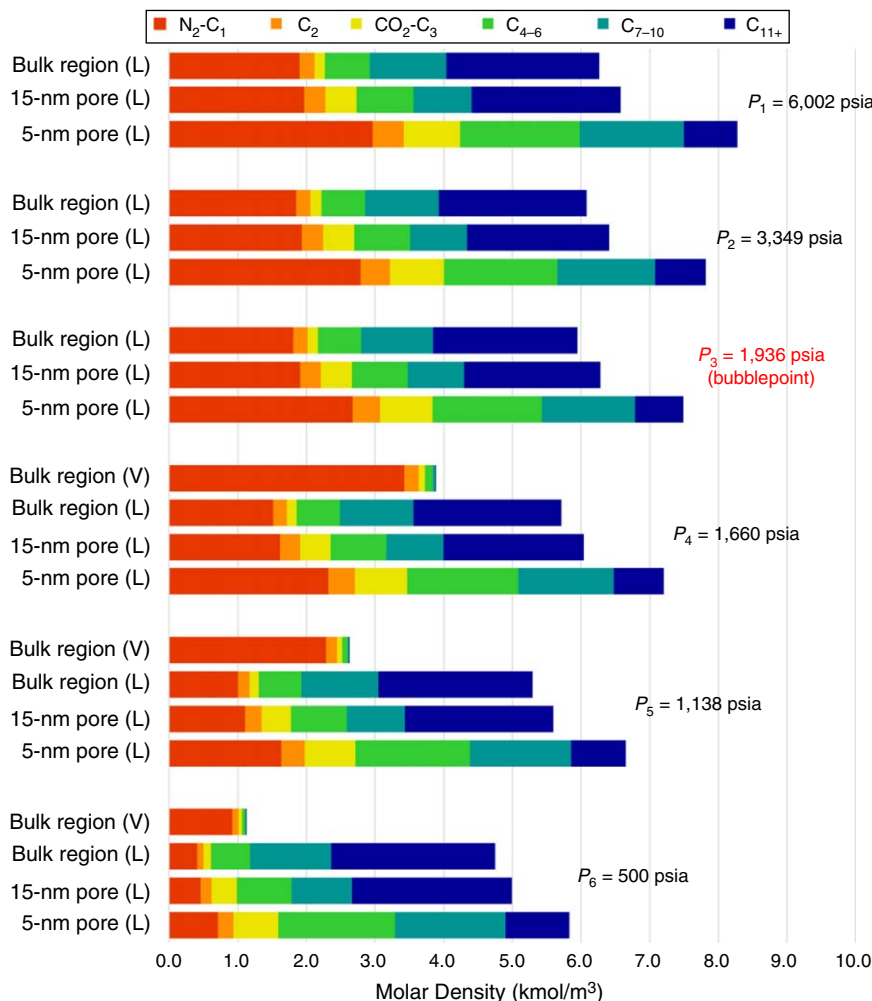

Fig. 11—Molar density profiles of all phases at selected pressures in the triple-scale CCE. The length of a cylinder section refers to the actual molar density (kmol/m³) of a specific species in the corresponding phase. The noted pressure is the bulk-region pressure. The bubblepoint pressure is 1,936 psia (138 psia lower than the conventional reservoir fluids), and the first bubble emerges from the bulk region. As the pressure is lowered, the gas phase expands in the bulk region, but the fluids are always undersaturated in 5- and 15-nm nanopores. The 5-nm pores have relatively high fractions of C_{1-6}. In the end, a significant amount of intermediate and heavy components are trapped in nanopores.
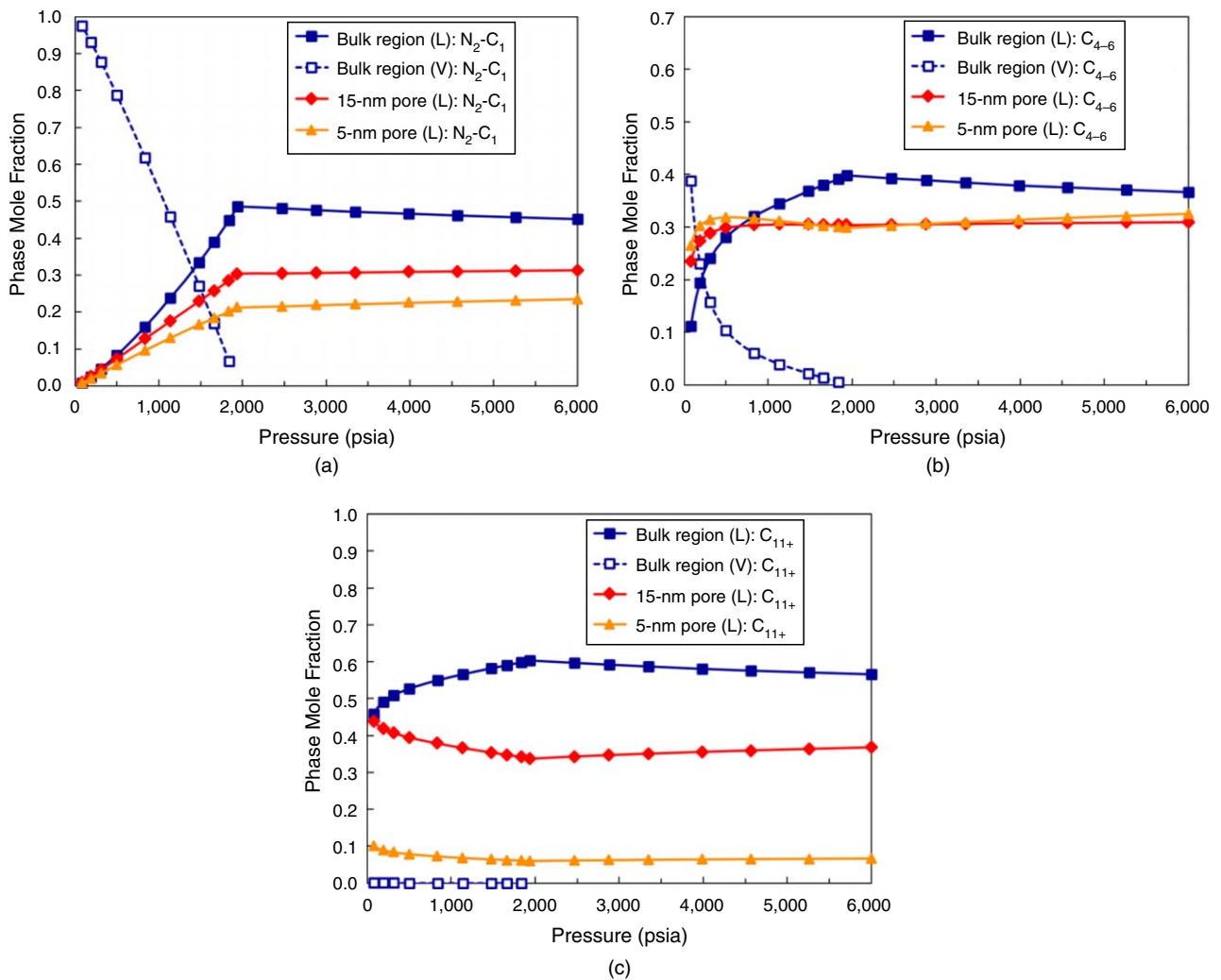
Fig. 12—Mole fractions of (a) light component, N_2-C_1, (b) intermediate component, C_{4-6}, and (c) heavy component, C_{11+}, distributed in various phases during the triple-scale CCE. The bubblepoint pressure is 1,936 psia. Below the bubblepoint, N_2-C_1 is quickly released from the bulk- and confined-liquid phases into the bulk-gas phase, and C_{4-6} is released into the gas phase from the nanopores at a very low pressure (approximately 300 psia). C_{11+} accumulates in the liquid phases of the nanopores (5 and 15 nm) below the bubblepoint. The phase mole fraction relates to the mole fraction of a species distributed in a certain phase.

The oil properties are also investigated by examining the critical temperature. For each stage in the CCE, the critical temperature of the fluid in a specific size of pore is calculated from Eqs. 16 and 17 (Firoozabadi 2015). Above the bubblepoint ($P > 1,936$ psia), the critical temperature of the liquid-state fluid in the nanopores (15 and 5 nm) is lower than those in the bulk region. The decreased critical temperature in nanopores is caused by both increased fractions of light and intermediate hydrocarbons and the nanoconfinement effect. Investigating the fluid in the 5-nm pores, the same composition at bulk state yields a critical temperature of 337°F. However, in the 5-nm pores, the critical point is further lowered to 263°F by the nanoconfinement effect. In this scenario, the critical temperature is slightly above the reservoir temperature (240°F), thus it is near-critical volatile oil in the 5-nm pore **(Fig. 13).** The decrease of the critical temperature in nanopores is consistent with previous findings from adsorption experiments (Thommes and Findenegg 1994) and molecular simulations (Singh et al. 2010; Jin and Nasrabadi 2016). By DSC, we also observed that the supercriticality of hydrocarbons was induced by confinement effects in the nanopores less than approximately 4 nm in diameter (Luo et al. 2016a). Below the bubblepoint, the critical temperature in the nanopores increases with decreasing pressure and the liquid-state fluid in the nanopores becomes richer in heavy hydrocarbons. In 5-nm pores, the compositional change is so large that it ultimately turns the fluid to black oil. As the fluid composition changes in the nanopores, the viscosity is expected to alter notably, which should significantly affect the fluid flow during the later stage of production in liquid-rich shale.

$$\left(\frac{\partial P}{\partial v}\right)_{T_C} = \left(\frac{\partial^2 P}{\partial v^2}\right)_{T_C} = 0, \quad \dots\dots\dots\dots\dots\dots\dots\dots\dots\dots\dots\dots\dots\dots\dots\dots\dots\dots\dots \quad (16)$$

$$\left(\frac{\partial^3 P}{\partial v^3}\right)_{T_C} < 0. \quad \dots\dots\dots\dots\dots\dots\dots\dots\dots\dots\dots\dots\dots\dots\dots\dots\dots\dots\dots\dots\dots\dots\dots \quad (17)$$

The liquid volumetric saturation/pressure behavior in the triple-scale system (bulk, 15 nm, and 5 nm) is similar to the dual-scale behavior. The bubblepoint (1,936 psia) is suppressed, and the liquid saturation decreases as the bulk region fluid enters the two-phase state **(Fig. 14a).** The effect on production GOR can be referred to the discussions in the Dual-Scale PVT subsection. The bulk region expands remarkably with decreasing pressure, and by assumption, the volumes of the nanopores are fixed (Fig. 14b).
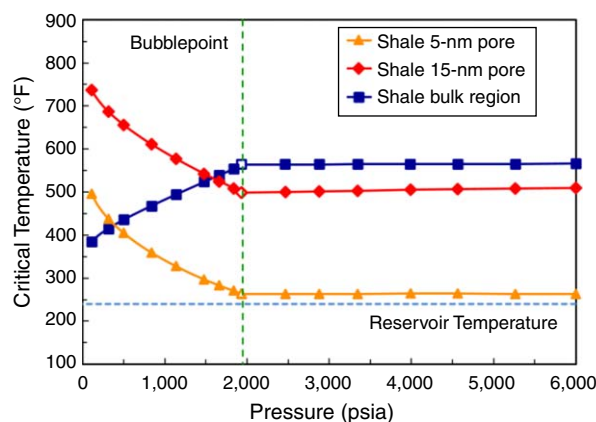
Fig. 13—Critical temperatures of fluid in the bulk region/nanopores with respect to pressure over the CCEs. The reservoir temperature is 240°F (light blue dashed line, horizontal) and the bubblepoint is 1,936 psia (green dashed line, vertically crossing the open symbols). At the undersaturated stage, the fluid in 5-nm pores is (near-critical) volatile oil. As the pressure falls below the bubblepoint, the fluid critical temperature in 5-nm pores shifts away from the reservoir temperature, and the fluid type turns into black oil.
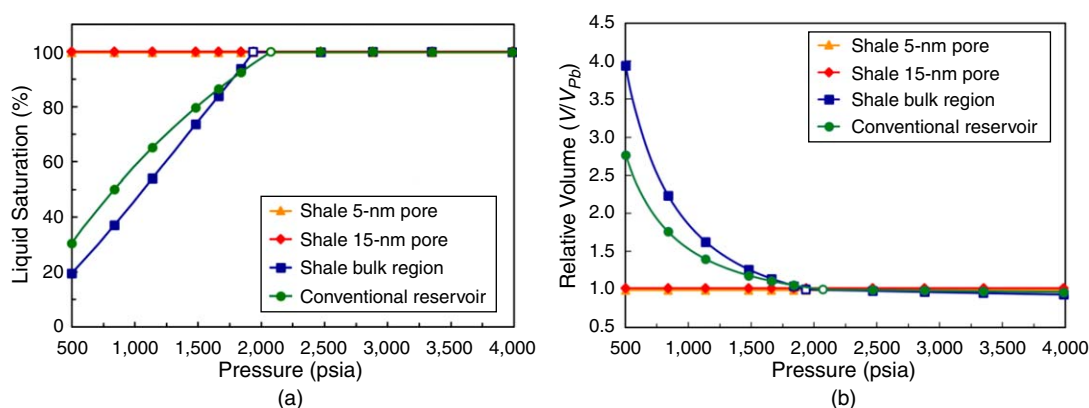

Fig. 14—(a) Liquid volumetric saturation of each region in relation to pressure. In the bulk region, P_b is suppressed, and the liquid saturation declines faster than that in the conventional reservoir. In nanopores (5 and 15 nm), the fluid is undersaturated at all pressures. (b) Pressure/volume relations. The nanopore volumes (5 and 15 nm) are fixed. The bulk region expands with lowered pressure at a rate faster than that in conventional reservoirs. The bubblepoint pressure for shale is marked as an open blue square, and for conventional reservoirs it is marked as a green circle.

Apparent Bubblepoint. The reservoir fluids behave quite differently in the broad pore-size distribution (nanometers to a few micrometers) of the shale porous structure. The fluid-evaporation/condensation pressure in nanopores is commonly lower than the bulk-saturation pressure because of the confinement effect. The lowered phase-transition pressures of pure fluids in nanocapillaries have been well-recorded in isothermal adsorption experiments (Thommes et al. 2002; Russo et al. 2011) and simulation studies (Walton and Quirke 1989). For the multicomponent shale-reservoir fluids, the vaporization in nanopores is further suppressed by the compositional extraction of light components (such as C_1 and C_2) into the gas phase of the bulk region. In the simulated CCE, the liquid/vapor transitions are completely suppressed in 5- and 15-nm pores; i.e., the fluids in the nanopores are undersaturated throughout the reservoir depletion. On the other hand, the first bubble of shale oil emerges from the bulk region at a deviated pressure from the single-scale bulk bubblepoint.

For the multiscale shale system, we suggest the term "apparent bubblepoint pressure" as the pressure when the first bubble forms in a certain region of scale while the fluids in the remaining regions stay undersaturated. In the case of Eagle Ford oil, the first bubble always occurs in the bulk region while the fluids in nanopores remain in the liquid state. As discussed, the apparent bubblepoint is associated with the onset of two-phase flow in the bulk porous geometries of shale (e.g., fractures) and the sharp rise of production GOR.

The apparent bubblepoint is rationalized to be dependent on the compositional distributions between the bulk region and nanopores. Because of the compositional heterogeneities, the apparent bubblepoint that occurs in the bulk region is slightly suppressed in the bulk/15-nm case (Fig. 7). With the small-scale nanopores (e.g., 5 nm), the bubblepoint is further suppressed (Fig. 11). The apparent bubblepoint pressures in shale are 2,002 psia for the bulk/15-nm case and 1,936 psia for the bulk/15-nm/5-nm case, which are lower than the bulk bubblepoint in the conventional reservoir (2,074 psia). It should be noted that the bubblepoint decrease of approximately 100 psi is almost within experimental uncertainty. However, we suggest the important findings are that there are no bubblepoints in nanopores in shale reservoirs.

At last, we conduct the sensitivity analysis of apparent bubblepoint to the volume percentages of nanoporous geometries. Herein, the volume ratio of 15-nm/5-nm pores is fixed as 2:1, but the volume percentage of nanopores in the total porous space is changed. The same feed of fluid (Tables 1 and 2) and initial reservoir conditions of 6,000 psia at 240°F are used. Shown in **Fig. 15,** the apparent bubblepoint is highly dependent on the volume percentage of nanopores. In the cases with less than 20% nanopores, the decrease of bubblepoint pressure is minor (50 psi or less); with moderate percentages of nanopores (30 to 60%), the bubblepoint decreases 100 to 150 psi; when the nanopores constitute the major porosity of porous media (>70%), the bubblepoint decreases more than 200 psi.
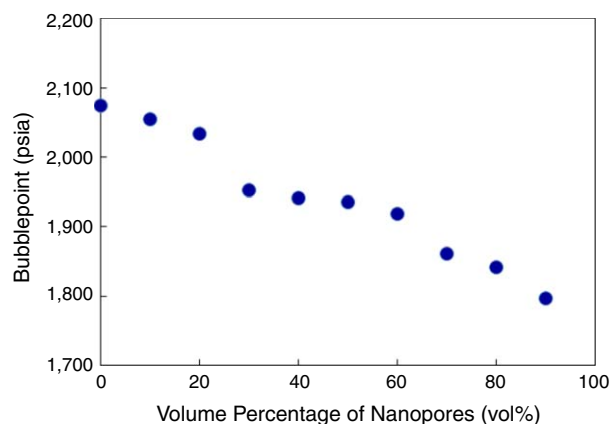
Fig. 15—Bubblepoint pressure in relation to the initial volume percentage of nanopores. The initial system is at 6,000 psia. 50 vol% corresponds to the triple-scale case presented previously. The 0 vol% of nanopores is equal to the single-scale bulk case. For the volume distribution of different nanopores, the ratio of 15-nm/5-nm pores is fixed as 2:1.

Conclusions

We have presented a simulation of phase equilibria of multicomponent reservoir fluids in shale reservoirs bearing multiple pore sizes (nanometer scale to bulk scale). On the basis of fluid phase behavior, the porous geometries of liquid-rich shale are divided into the bulk region (>50 nm; e.g., fractures and macropores) and nanopores (<50 nm). A pore-size-dependent EOS (Travalloni et al. 2014) extended from PR EOS is used to describe the fluid in each region by pore diameter. The confinement parameters (square-well potential depth and width for the fluid/pore-surface interaction) of the EOS are determined by experimental phase transition pressures/temperatures in organo-functionalized nanoporous silica. The experimental porous media possess analogous surface properties with organic matter in shale. The multiscale phase equilibria are calculated by global minimization of Helmholtz free energy. A case of modified Eagle Ford oil is studied. Our multiscale PVT model gives results consistent with those of commercial software on single-scale bulk fluids. The dual-scale (bulk and 15 nm) and triple-scale (bulk, 15 nm, and 5 nm) CCEs are simulated. The fluid compositions and criticalities are examined. The following are the main findings and conclusions of this study:

1. In initially undersaturated multiscale systems, the first bubble forms in the bulk-scale region (fractures, macropores) while the fluids in nanopores remain undersaturated. The transition pressure is noted as the apparent bubblepoint.
2. The apparent bubblepoint pressure of fluids in shale depends on compositional distributions between the bulk region and nanopores. Simulations using the confinement parameters of an organic-matter analog suggest a suppressed bubblepoint. The small-scale nanopores (e.g., 5 nm) or high volumetric fractions of nanopores lead to a further-shifted apparent bubblepoint.
3. Above the apparent bubblepoint pressure, the reservoir fluids in all regions are liquid. In the bulk region pores and 15-nm pores, the fluids are black oil. In 5-nm pores, the fluid is near-critical volatile oil with high fractions of light and intermediate components. The near-critical scenario is induced by the small-scale nanoconfinement effect.
4. As the pressure falls below the apparent bubblepoint, the gas phase expands in the bulk region. However, the fluids in nanopores (5 and 15 nm) remain undersaturated throughout the depletion. In 5-nm pores, the fluid transforms from volatile oil toward black oil by releasing the light hydrocarbons and absorbing the heavy ones.
5. In the two-phase stage, the liquid saturation drops quickly in the bulk region.
6. During depletion, the nanopores release light components and accumulate heavy ones. In the end, many intermediate-to-heavy components are retained in the nanopores in the form of undersaturated fluids.

Nomenclature

a = conventional energy parameter for PR EOS
a_p = confinement-modified energy parameter for PR-C EOS
A = Helmholtz free energy
b = conventional volume parameter for PR EOS
b_p = confinement-modified volume parameter for PR-C EOS
d = cylindrical pore diameter
$F_{pr,i}$ = fraction of fluid within the pore surface attractive field under random distribution
k_B = Boltzmann constant
k_{ij} = binary-interaction parameters between components i and j
n_i = mole number of component i
N_{av} = Avogadro's number
P = pressure
P_b = bubblepoint pressure
P_C = critical pressure
r_p = cylindrical pore radius
R = ideal-gas constant
T = temperature
T_C = critical temperature
v = molar volume
V = volume
x_i = mole fraction of component i
δ_p = square-well depth of fluid/pore-wall interaction potential
ε_p = square-well depth of fluid/pore-wall interaction potential

θ = geometric term in expression of F_p

κ = fluid/pore-surface affinity factor

λ = de Broglie wavelength

μ_i = chemical potential of component i

σ_i = molecular diameter of component i

ω = acentric factor

Acknowledgments

References

Alfi, M., Nasrabadi, H., and Banerjee, D. 2016. Experimental Investigation of Confinement Effect on Phase Behavior of Hexane, Heptane and Octane Using Lab-on-a-Chip Technology. *Fluid Phase Equilibr.* **423** (15 September): 25–33. https://doi.org/10.1016/j.fluid.2016.04.017.

Alharthy, N. S., Nguyen, T., Teklu, T. et al. 2013. Multiphase Compositional Modeling in Small-Scale Pores of Unconventional Shale Reservoirs. Presented at the SPE Annual Technical Conference and Exhibition, New Orleans, 30 September–2 October. SPE-166306-MS. https://doi.org/10.2118/166306-MS.

Anders, M. H., Laubach, S. E., and Scholz, C. H. 2014. Microfractures: A Review. *J. Struct. Geol.* **69B** (December): 377–394. https://doi.org/10.1016/j.jsg.2014.05.011.

Bear, J., Tsang, C.-F., and De Marsily, G. 1993. *Flow and Contaminant Transport in Fractured Rocks*. New York City: Academic Press.

Cabral, V. F., Castier, M., and Tavares, F. W. 2005. Thermodynamic Equilibrium in Systems With Multiple Adsorbed and Bulk Phases. *Chem. Eng. Sci.* **60** (6): 1773–1782. https://doi.org/10.1016/j.ces.2004.11.007.

Carley, D. D. 1983. Thermodynamic Properties of a Square-Well Fluid in the Liquid and Vapor Regions. *J. Chem. Phys.* **78** (9): 5776–5781. https://doi.org/10.1063/1.445462.

Chapela, G. A., Martínez-Casas, S. E., and Varea, C. 1987. Square Well Orthobaric Densities via Spinodal Decomposition. *J. Chem. Phys.* **86** (10): 5683–5688. https://doi.org/10.1063/1.452546.

Cho, Y., Eker, E., Uzun, I. et al. 2016. Rock Characterization in Unconventional Reservoirs: A Comparative Study of Bakken, Eagle Ford, and Niobrara Formations. Presented at the SPE Low Perm Symposium, Denver, 5–6 May. SPE-180239-MS. https://doi.org/10.2118/180239-MS.

Choi, E. S., Cheema, T., and Islam, M. R. 1997. A New Dual-Porosity/Dual-Permeability Model With Non-Darcian Flow Through Fractures. *J. Pet. Sci. Eng.* **17** (3): 331–344. https://doi.org/10.1016/S0920-4105(96)00050-2.

Civan, F., Michel, G., and Sigal, R. 2013. Impact of Fluid Behavior Modification Under Elevated Pressure and Temperature Conditions on Shale-Gas/Condensate Reservoir Engineering and Production Analysis. Presented at the SPE Unconventional Resources Conference Canada, Calgary, 5–7 November. SPE-167186-MS. https://doi.org/10.2118/167186-MS.

Dahi-Taleghani, A. and Olson, J. E. 2011. Numerical Modeling of Multistranded-Hydraulic-Fracture Propagation: Accounting for the Interaction Between Induced and Natural Fractures. *SPE J.* **16** (3): 575–581. SPE-124884-PA. https://doi.org/10.2118/124884-PA.

Dong, X., Liu, H., Hou, J. et al. 2016. Phase Equilibria of Confined Fluids in Nanopores of Tight and Shale Rocks Considering the Effect of Capillary Pressure and Adsorption Film. *Ind. Eng. Chem. Res.* **55** (3): 798–811. https://doi.org/10.1021/acs.iecr.5b04276.

Du, L. and Chu, L. 2012. Understanding Anomalous Phase Behavior in Unconventional Oil Reservoirs. Presented at the Canadian Unconventional Resources Conference, Calgary, 30 October–1 November. SPE-161830-MS. https://doi.org/10.2118/161830-MS.

Firoozabadi, A. 2015. *Thermodynamics and Applications of Hydrocarbons Energy Production*, first edition. New York City: McGraw-Hill Education.

Floquet, N., Coulomb, J. P., Llewellyn, P. L. et al. 2007. Adsorption and Neutron Scattering Studies: A Reliable Way to Characterize Both the Mesoporous MCM-41 and the Filling Mode of the Adsorbed Species. *Stud. Surf. Sci. Catal.* **160:** 71–78. https://doi.org/10.1016/S0167-2991(07)80011-5.

Gale, J. F., Laubach, S. E., Olson, J. E. et al. 2014. Natural Fractures in Shale: A Review and New Observations. *AAPG Bull.* **98** (11): 2165–2216. https://doi.org/10.1306/08121413151.

Gale, J. F. W., Reed, R. M., and Holder, J. 2007. Natural Fractures in the Barnett Shale and Their Importance for Hydraulic Fracture Treatments. *AAPG Bull.* **91** (4): 603–622. https://doi.org/10.1306/11010606061.

Gilman, J. R., Kazemi, H. 1983. Improvements in Simulation of Naturally Fractured Reservoirs. *Society of Petroleum Engineers Journal* **23** (04): 695–707.

Günther, G., Prass, J., Paris, O. et al. 2008. Novel Insights Into Nanopore Deformation Caused by Capillary Condensation. *Phys. Rev. Lett.* **101** (8): 086104. https://doi.org/10.1103/PhysRevLett.101.086104.

Honarpour, M. M., Nagarajan, N. R., Orangi, A. et al. 2012. Characterization of Critical Fluid PVT, Rock, and Rock-Fluid Properties—Impact on Reservoir Performance of Liquid Rich Shales. Presented at the SPE Annual Technical Conference and Exhibition, San Antonio, Texas, 8–10 October. SPE-158042-MS. https://doi.org/10.2118/158042-MS.

Hu, Y., Devegowda, D., Striolo, A. et al. 2014. Microscopic Dynamics of Water and Hydrocarbon in Shale-Kerogen Pores of Potentially Mixed Wettability. *SPE J.* **20** (1): 112–124. SPE-167234-PA. https://doi.org/10.2118/167234-PA.

Jin, B. and Nasrabadi, H. 2016. Phase Behavior of Multi-Component Hydrocarbon Systems in Nano-Pores Using Gauge-GCMC Molecular Simulation. *Fluid Phase Equilibr.* **425** (15 October): 324–334. https://doi.org/10.1016/j.fluid.2016.06.018.

Jin, Z. and Firoozabadi, A. 2016. Thermodynamic Modeling of Phase Behavior in Shale Media. *SPE J.* **21** (1): 190–207. SPE-176015-PA. https://doi.org/10.2118/176015-PA.

Jones, R. S. Jr. 2017. Producing-Gas/Oil-Ratio Behavior of Multifractured Horizontal Wells in Tight Oil Reservoirs. *SPE Res Eval & Eng* **20** (3): 589–601. SPE-184397-PA. https://doi.org/10.2118/184397-PA.

Ko, L. T., Loucks, R. G., Ruppel, S. C. et al. 2017. Origin and Characterization of Eagle Ford Pore Networks in the South Texas Upper Cretaceous Shelf. *AAPG Bull.* **101** (3): 387–418. https://doi.org/10.1306/08051616035.

Kuila, U. and Prasad, M. 2013. Specific Surface Area and Pore-Size Distribution in Clays and Shales. *Geophys. Prospect.* **61** (2): 341–362. https://doi.org/10.1111/1365-2478.12028.

Kuraoka, K., Chujo, Y., and Yazawa, T. 2001. Hydrocarbon Separation via Porous Glass Membranes Surface-Modified Using Organosilane Compounds. *J. Membrane Sci.* **182** (1–2): 139–149. https://doi.org/10.1016/S0376-7388(00)00559-7.

Li, Z., Jin, Z., and Firoozabadi, A. 2014. Phase Behavior and Adsorption of Pure Substances and Mixtures and Characterization in Nanopore Structures by Density Functional Theory. *SPE J.* **19** (6): 1096–1109. SPE-169819-PA. https://doi.org/10.2118/169819-PA.

Loucks, R. G., Reed, R. M., Ruppel, S. C. et al. 2009. Morphology, Genesis, and Distribution of Nanometer-Scale Pores in Siliceous Mudstones of the Mississippian Barnett Shale. *J. Sediment. Res.* **79** (12): 848–861. https://doi.org/10.2110/jsr.2009.092.

Lourenço, M. A. O., Siquet, C., Sardo, M. et al. 2016. Interaction of CO_2 and CH_4 With Functionalized Periodic Mesoporous Phenylene–Silica: Periodic DFT Calculations and Gas Adsorption Measurements. *J. Phys. Chem. C* **120** (7): 3863–3875. https://doi.org/10.1021/acs.jpcc.5b11844.

Luo, S., Lutkenhaus, J. L., Nasrabadi, H. 2015. Experimental Study of Confinement Effect on Hydrocarbon Phase Behavior in Nanoscale Porous Media Using Differential Scanning Calorimetry. Presented at the SPE Annual Technical Conference and Exhibition, Houston, 28–30 September. SPE-175095-MS. https://doi.org/10.2118/175095-MS.

Luo, S., Lutkenhaus, J. L., and Nasrabadi, H. 2016a. Confinement-Induced Supercriticality and Phase Equilibria of Hydrocarbons in Nanopores. *Langmuir* **32** (44): 11506–11513. https://doi.org/10.1021/acs.langmuir.6b03177.

Luo, S., Lutkenhaus, J. L., and Nasrabadi, H. 2016b. Use of Differential Scanning Calorimetry to Study Phase Behavior of Hydrocarbon Mixtures in Nanoscale Porous Media. *J. Pet. Sci. Eng.* **163** (April): 731–738. https://doi.org/10.1016/j.petrol.2016.12.019.

Luo, S., Nasrabadi, H., and Lutkenhaus, J. L. 2016c. Effect of Confinement on the Bubble Points of Hydrocarbons in Nanoporous Media. *AlChE J.* **62** (5): 1772–1780. https://doi.org/10.1002/aic.15154.

Matsumoto, A., Misran, H., and Tsutsumi, K. 2004. Adsorption Characteristics of Organosilica Based Mesoporous Materials. *Langmuir* **20** (17): 7139–7145. https://doi.org/10.1021/la0360409.

Naumov, S., Valiullin, R., Monson, P. A. et al. 2008. Probing Memory Effects in Confined Fluids via Diffusion Measurements. *Langmuir* **24** (13): 6429–6432. https://doi.org/10.1021/la801349y.

Nichita, D. V., Gomez, S., and Luna, E. 2002. Multiphase Equilibria Calculation by Direct Minimization of Gibbs Free Energy With a Global Optimization Method. *Comput. Chem. Eng.* **26** (12): 1703–1724. https://doi.org/10.1016/S0098-1354(02)00144-8.

Nichita, D. V., de los Angeles Duran Valencia, C., and Gomez, S. 2006. Volume-Based Thermodynamics Global Phase Stability Analysis. *Chem. Eng. Commun.* **193** (10): 1194–1216. https://doi.org/10.1080/00986440500440165.

Nojabaei, B., Johns, R. T., and Chu, L. 2013. Effect of Capillary Pressure on Phase Behavior in Tight Rocks and Shales. *SPE J.* **16** (3): 281–289. SPE-159258-PA. https://doi.org/10.2118/159258-PA.

Orangi, A., Nagarajan, N. R., Honarpour, M. M. et al. 2011. Unconventional Shale Oil and Gas-Condensate Reservoir Production, Impact of Rock, Fluid, and Hydraulic Fractures. Presented at the SPE Hydraulic Fracturing Technology Conference, The Woodlands, Texas, 24–26 January. SPE-140536-MS. https://doi.org/10.2118/140536-MS.

Peng, D. Y. and Robinson, D. B. 1976. A New Two-Constant Equation of State. *Ind. Eng. Chem. Fundamen.* **15** (1): 59–64. https://doi.org/10.1021/i160057a011.

Rouquerol, J., Avnir, D., Fairbridge, C. W. et al. 1994. Recommendations for the Characterization of Porous Solids (Technical Report). *Pure Appl. Chem.* **66** (8): 1739–1758.

Russo, P. A., Carrott, M. M. L. R., and Carrott, P. J. M. 2011. Hydrocarbons Adsorption on Templated Mesoporous Materials: Effect of the Pore Size, Geometry and Surface Chemistry. *New J. Chem.* **35** (2): 407–416. https://doi.org/10.1039/C0NJ00614A.

Sandler, S. I. 2010. The Generalized van der Waals Partition Function as a Basis for Excess Free Energy Models. *J. Supercrit. Fluid.* **55** (2): 496–502. https://doi.org/10.1016/j.supflu.2010.10.014.

Sing, K. S. W., Everett, D. H., Haul, R. A. W. et al. 1985. Reporting Physisorption Data for Gas/Solid Systems With Special Reference to the Determination of Surface Area and Porosity (Recommendations 1984). *Pure Appl. Chem.* **57** (4): 603–619.

Singh, S. K. and Singh, J. K. 2011. Effect of Pore Morphology on Vapor–Liquid Phase Transition and Crossover Behavior of Critical Properties From 3D to 2D. *Fluid Phase Equilibr.* **300** (1–2): 182–187. https://doi.org/10.1016/j.fluid.2010.10.014.

Singh, S. K., Saha, A. K., and Singh, J. K. 2010. Molecular Simulation Study of Vapor-Liquid Critical Properties of a Simple Fluid in Attractive Slit Pores: Crossover From 3D to 2D. *J. Phys. Chem. B* **114** (12): 4283–4292. https://doi.org/10.1021/jp9109942.

Singh, S. K., Sinha, A., Deo, G. et al. 2009. Vapor-Liquid Phase Coexistence, Critical Properties, and Surface Tension of Confined Alkanes. *J. Phys. Chem. C* **113** (17): 7170–7180. https://doi.org/10.1021/jp8073915.

Tan, S. P. and Piri, M. 2015a. Equation-of-State Modeling of Associating-Fluids Phase Equilibria in Nanopores. *Fluid Phase Equilibr.* **405** (15 November): 157–166. https://doi.org/10.1016/j.fluid.2015.07.044.

Tan, S. P. and Piri, M. 2015b. Equation-of-State Modeling of Confined-Fluid Phase Equilibria in Nanopores. *Fluid Phase Equilibr.* **393** (15 May): 48–63. https://doi.org/10.1016/j.fluid.2015.02.028.

Thommes, M. and Findenegg, G. H. 1994. Pore Condensation and Critical-Point Shift of a Fluid in Controlled-Pore Glass. *Langmuir* **10** (11): 4270–4277. https://doi.org/10.1021/la00023a058.

Thommes, M., Köhn, R., and Fröba, M. 2002. Sorption and Pore Condensation Behavior of Pure Fluids in Mesoporous MCM-48 Silica, MCM-41 Silica, SBA-15 Silica and Controlled-Pore Glass at Temperatures Above and Below the Bulk Triple Point. *Appl. Surf. Sci.* **196** (1–4): 239–249. https://doi.org/10.1016/S0169-4332(02)00062-4.

Travalloni, L., Castier, M., and Tavares, F. W. 2014. Phase Equilibrium of Fluids Confined in Porous Media From an Extended Peng-Robinson Equation of State. *Fluid Phase Equilibr.* **362** (25 January): 335–341. https://doi.org/10.1016/j.fluid.2013.10.049.

Travalloni, L., Castier, M., Tavares, F. W. et al. 2010a. Critical Behavior of Pure Confined Fluids From an Extension of the van der Waals Equation of State. *J. Supercrit. Fluid.* **55** (2): 455–461. https://doi.org/10.1016/j.supflu.2010.09.008.

Travalloni, L., Castier, M., Tavares, F. W. et al. 2010b. Thermodynamic Modeling of Confined Fluids Using an Extension of the Generalized van der Waals Theory. *Chem. Eng. Sci.* **65** (10): 3088–3099. https://doi.org/10.1016/j.ces.2010.01.032.

Vega, L., de Miguel, E., Rull, L. F. et al. 1992. Phase Equilibria and Critical Behavior of Square-Well Fluids of Variable Width by Gibbs Ensemble Monte Carlo Simulation. *J. Chem. Phys.* **96** (3): 2296–2305. https://doi.org/10.1063/1.462080.

Vera, J. H. and Prausnitz, J. M. 1972. Generalized van der Waals Theory for Dense Fluids. *Chem. Eng. J.* **3:** 1–13. https://doi.org/10.1016/0300-9467(72)85001-9.

Walton, J. P. R. B. and Quirke, N. 1989. Capillary Condensation: A Molecular Simulation Study. *Mol. Simulat.* **2** (4–6): 361–391. https://doi.org/10.1080/08927028908034611.

Wang, L., Yin, X., Neeves, K. B. et al. 2016. Effect of Pore-Size Distribution on Phase Transition of Hydrocarbon Mixtures in Nanoporous Media. *SPE J.* **21** (6): 1981–1995. SPE-170894-PA. https://doi.org/10.2118/170894-PA.

Warpinski, N. 1985. Measurement of Width and Pressure in a Propagating Hydraulic Fracture. *SPE J.* **25** (1): 46–54. SPE-11648-PA. https://doi.org/10.2118/11648-PA.

Warren, J. and Root, P. J. 1963. The Behavior of Naturally Fractured Reservoirs. *SPE J.* **3** (3): 245–255. SPE-426-PA. https://doi.org/10.2118/426-PA.

Whitson, C. H. and Sunjerga, S. 2012. PVT in Liquid-Rich Shale Reservoirs. Presented at the SPE Annual Technical Conference and Exhibition, San Antonio, Texas, 8–10 October. SPE-155499-MS. https://doi.org/10.2118/155499-MS.

Zhang, Y., Yu, W., Sepehrnoori, K. et al. 2017. Investigation of Nanopore Confinement on Fluid Flow in Tight Reservoirs. *J. Pet. Sci. Eng.* **150** (February): 265–271. https://doi.org/10.1016/j.petrol.2016.11.005.

Zhao, X. S. and Lu, G. Q. 1998. Modification of MCM-41 by Surface Silylation With Trimethylchlorosilane and Adsorption Study. *J. Phys. Chem. B* **102** (9): 1556–1561. https://doi.org/10.1021/jp972788m.

Zhu, H. Y., Ni, L. A., and Lu, G. Q. 1999. A Pore-Size-Dependent Equation of State for Multilayer Adsorption in Cylindrical Mesopores. *Langmuir* **15** (10): 3632–3641. https://doi.org/10.1021/la981515v.

Appendix A—PR-C EOS

The PR-C EOS is written as follows (Travalloni et al. 2014):

$$P = \frac{RT}{v - b_p} - \frac{a_p}{v^2 + 2b_p v - b_p^2} - \sum_{i=1}^{NC}\left(\frac{x_i^2 \theta_i b_{p,i}}{v^2}\left(1 - \frac{x_i b_{p,i}}{v}\right)^{\theta_i - 1}(1 - F_{pr,i})\left\{ RT\left[1 - \exp\left(-\frac{N_{av}\varepsilon_{p,i}}{RT}\right)\right] - N_{av}\varepsilon_{p,i}\right\}\right), \quad \ldots \ldots \text{(A-1)}$$

$$\mu_i = \mu_{0,i} + RT\ln\left(\frac{N_{av}x_i\lambda_i^3}{v - b_p}\right) + \frac{RTb_{p,i}}{v - b_p} - \frac{a_p b_{p,i} v}{b_p(v^2 + 2b_p v - b_p^2)} + \frac{\sqrt{2}}{4}\ln\left[\frac{v + (1 + \sqrt{2})b_p}{v + (1 - \sqrt{2})b_p}\right]\left[\frac{a_p b_{p,i}}{b_p^2} - \frac{2}{b_p}\sum_{j=1}^{NC}(x_j a_{p,ij})\right] - F_{pr,i}N_{av}\varepsilon_{p,i}$$

$$+ \left[1 - (\theta_i + 1)\frac{x_i b_{p,i}}{v}\right]\left(1 - \frac{x_i b_{p,i}}{v}\right)^{\theta_i - 1}(1 - F_{pr,i})\left\{RT\left[1 - \exp\left(-\frac{N_{av}\varepsilon_{p,i}}{RT}\right)\right] - N_{av}\varepsilon_{p,i}\right\}, \quad \ldots \ldots \ldots \ldots \text{(A-2)}$$

where a_p and b_p are confinement-modified energy and volume parameters for EOS; r_p is the cylindrical pore radius; σ_i is the molecular diameter of component i from Eq. A-8; and σ_{ij} is the average molecular diameter of components i and j from Eq. A-9. The binary-interaction parameters k_{ij} are included in the mixing rule (Eq. A-5). a_p is given as

$$m_i = \begin{cases} 0.37464 + 1.54226\omega_i - 0.26992\omega_i^2, & 0 < \omega_i \le 0.5 \\ 0.3796 + 1.485\omega_i - 0.1644\omega_i^2 + 0.01667\omega_i^3, & \omega_i > 0.5, \end{cases} \quad \ldots \ldots \ldots \ldots \ldots \text{(A-3)}$$

$$a_i = \frac{0.45724R^2 T_{C,i}^2}{P_{C,i}}\left[1 + m_i\left(1 - \sqrt{\frac{T}{T_{C,i}}}\right)\right]^2, \quad \ldots \ldots \ldots \ldots \ldots \ldots \text{(A-4)}$$

$$a_{p,ij} = (1 - k_{ij})\sqrt{a_i a_j}\left(1 - \frac{2}{5}\frac{\sigma_{ij}}{r_p}\right), \quad \ldots \ldots \ldots \ldots \ldots \ldots \text{(A-5)}$$

$$a_p = \sum_{i=1}^{NC}\sum_{j=1}^{NC}(x_i x_j a_{p,ij}). \quad \ldots \ldots \ldots \ldots \ldots \ldots \text{(A-6)}$$

b_p is given as

$$b_i = \frac{0.07780RT_{C,i}}{P_{C,i}}, \quad \ldots \ldots \ldots \ldots \ldots \ldots \ldots \ldots \text{(A-7)}$$

$$\sigma_i = \sqrt[3]{\frac{1.158b_i}{N_{av}}}, \quad \ldots \ldots \ldots \ldots \ldots \ldots \ldots \ldots \text{(A-8)}$$

$$\sigma_{ij} = \frac{\sigma_i + \sigma_j}{2}, \quad \ldots \ldots \ldots \ldots \ldots \ldots \ldots \ldots \text{(A-9)}$$

$$b_{p,i} = \frac{N_{av}\sigma_i^3}{1.158 - 0.479\exp\left[0.621\left(0.5 - \frac{r_p}{\sigma_i}\right)\right] + 0.595\exp\left[4.014\left(0.5 - \frac{r_p}{\sigma_i}\right)\right]}, \quad \ldots \ldots \ldots \ldots \text{(A-10)}$$

$$b_p = \sum_{i=1}^{NC} x_i b_{p,i}. \quad \ldots \ldots \ldots \ldots \ldots \ldots \ldots \ldots \text{(A-11)}$$

For component i, θ_i is the geometric term and $F_{pr,i}$ is the fraction of fluid within the pore surface attractive field under random distribution:

$$\theta_i = \frac{r_p}{\delta_{p,i} + \frac{\sigma_i}{2}}, \quad \ldots \ldots \ldots \ldots \ldots \ldots \ldots \ldots \text{(A-12)}$$

$$F_{pr,i} = \frac{\left(r_p - \frac{\sigma_i}{2}\right)^2 - \left(r_p - \frac{\sigma_i}{2} - \delta_{p,i}\right)^2}{\left(r_p - \frac{\sigma_i}{2}\right)^2}. \quad \ldots \ldots \ldots \ldots \ldots \ldots \text{(A-13)}$$

Sheng Luo is a PhD degree candidate in the Harold Vance Department of Petroleum Engineering at Texas A&M University. His research interests include phase behavior of fluids in nanopores, adsorption, gas injection, and compositional simulation. Luo holds a bachelor's degree from Tsinghua University, Beijing, and a master's degree from the University of Texas Southwestern Medical Center, both in chemistry.

Jodie L. Lutkenhaus is the William and Ruth Neely Faculty Fellow and an associate professor in the Artie McFerrin Department of Chemical Engineering at Texas A&M University. Her research interests include fluids in confinement, polymers, corrosion, and energy storage. Lutkenhaus has authored or coauthored more than 75 technical papers. She holds a PhD degree in chemical engineering from the Massachusetts Institute of Technology.

Hadi Nasrabadi is the Douglas Von Gonten Faculty Fellow and an assistant professor in the Harold Vance Department of Petroleum Engineering at Texas A&M University. His current research interests include hydrocarbon-phase behavior and flow in nanoscale porous media and molecular simulation. Nasrabadi holds a bachelor's degree in civil engineering from Sharif University of Technology, Iran, and a PhD degree in petroleum engineering from Imperial College London.